The viscoplastic Stokes layer

Neil J. Balmforth[a,b], Y. Forterre[c], O. Pouliquen[c,*]

[a] Department of Mathematics, University of British Columbia, Vancouver, Canada
[b] Department of Earth & Ocean Science, University of British Columbia, Vancouver, Canada
[c] Laboratoire I.U.S.T.I - UMR 6595 CNRS - Aix Marseille Université (UI,UII), 5 rue Enrico Fermi, 13013 Marseille, France

ARTICLE INFO

ABSTRACT

A theoretical and experimental study is presented of the viscoplastic version of the Stokes problem, in which a oscillating wall sets an overlying fluid layer into one-dimensional motion. For the theory, the fluid is taken to be described by the Herschel–Bulkley constitutive law, and the flow problem is analogous to an unusual type of Stefan problem. In the theory, when the driving oscillations are relatively weak, the overlying viscoplastic layer moves rigidly with the plate. For sufficiently strong oscillations, the fluid yields and numerical solutions illustrate how localized plug regions coexist with sheared regions and migrate vertically through the fluid layer. For the experiments, a layer of kaolin slurry in a rectangular tank is driven sinusoidally back and forth. The experiments confirm the threshold for shearing flow, equivalent to a balance between inertia and yield-stress. However, although kaolin is well described by a Herschel–Bulkley rheology, the layer dynamics notably differs between theory and experiments, revealing rheological behaviour not captured by the steady flow rule.

© 2008 Elsevier B.V. All rights reserved.

1. Introduction

The Stokes layer (the development of motion in a viscous fluid adjacent to an oscillating wall) is a classical problem in fluid mechanics, and appears in most textbooks on the subject (*e.g.* [1]; the oscillating plate problem is sometimes referred to as Stokes' second problem). The fluid dynamics is simplified significantly in this problem by virtue of the one-dimensionality of the flow, and general solutions can be given for viscous fluids even when the wall motion is arbitrary (although the solution takes an integral form). The most recent literature on the Stokes problem is directed towards the flow instabilities that occur at higher Reynolds number [2], applications in microfluidics [3] or to its extensions for viscoelastic fluids [4,5].

For a viscous layer of thickness, h, adjacent to an oscillating wall with frequency, ω, and speed, $-U \cos \omega t$, the surface speed of the fluid in the laboratory frame, $V(t)$, can be shown to satisfy (over times sufficiently long that the solution converges to a periodic signal)

$$\frac{V}{U} = -2 \frac{\cos \omega t \, ch(H/\sqrt{2}) \cos(H/\sqrt{2}) + \sin \omega t \, sh(H/\sqrt{2}) \sin(H/\sqrt{2})}{ch(H/\sqrt{2}) + \cos(H/\sqrt{2})},$$
(1)

where $H = h/\ell$, $\ell = \sqrt{\eta/\rho\omega}$ is the Stokes penetration depth, η is the dynamic viscosity and ρ is the density. When the thickness of the fluid layer is small compared with the Stokes length (small thickness, low frequency or high viscosity), the surface speed reduces to the base speed, whereas for $H \to \infty$ the surface speed becomes exponentially small. For arbitrary H, the velocity profile oscillates across the layer as sketched in Fig. 1 (left).

The purpose of the present article is to explore the viscoplastic version of the Stokes layer. The existence of a yield stress introduces a strong nonlinearity into the problem that, for most flow problems, significantly affects the dynamics. The most obvious difference with a viscous fluid is that for sufficiently gentle oscillations, the shear stress developed across the layer never reaches the yield stress and one expects the material to move rigidly with the base. On the other hand, there should also be a critical acceleration above which the shear stress at the base exceeds the yield stress, resulting in internal shearing and flow. This behaviour is reminiscent of the motion of a rigid block sliding frictionally over a moving plate. For such a system, the block is frictionally locked to the plate if

$$|\sin \omega t| < \frac{\mu g}{\omega U} \to V = -U \cos \omega t;$$
(2)

otherwise the block slides according to the equation of motion

$$\frac{dV}{dt} = -\mu g \; sgn(V + U \cos \omega t),$$
(3)

where μ is the solid friction coefficient between the block and the base (no distinction is made between static and dynamic friction)

* Corresponding author.
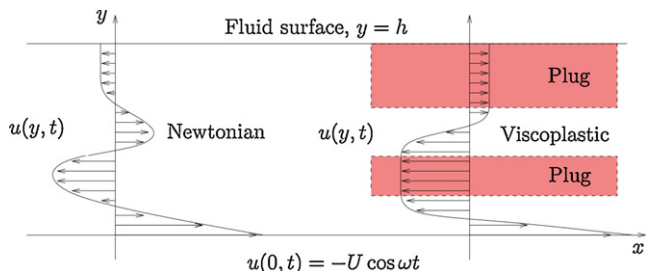 E-mail address: olivier.pouliquen@univ-provence.fr (O. Pouliquen).

Fig. 1. The set-up of the problem. On the left we sketch the flow field expected for the Newtonian problem (with the spatial oscillations emphasized); the picture to the right suggests how this flow field might be modified by the introduction of a yield stress.

and g is gravity. For $\mu g > \omega U$, friction is always sufficient to hold the block in place throughout the oscillation of the plate. When $\mu g < \omega U$, however, friction cannot hold the block in place for at least part of the cycle. Two types of behaviour then result. For higher friction, the block slides for only part of the cycle, and there is period of locking. At lower friction, the block slides for the whole cycle and executes an orbit with a sawtooth oscillation in $V(t)$, as illustrated in Fig. 2.

Although a viscoplastic fluid may behave like a sliding block close to the threshold, the dynamics is enriched by the ability of the material to yield and shear within the bulk and not just at the base. In particular, within the viscoplastic Stokes layer there may be a complicated structure to the yield surfaces that divide sheared flow from unyielded plugs. Notably, the dynamics of Newtonian Stokes layers corresponds to viscous diffusion, and the steady response to an oscillating wall takes the form of a velocity field that decays exponentially and oscillates in space as one ascends through the fluid (Fig. 1, left). The oscillatory signal emphasizes how the shear rate passes periodically through zero, a situation that leads one to suspect that a yield stress will generate a sequence of localized plugs over the low-shear-rate regions. The sketch on the right of Fig. 1 illustrates the notion.

Our goal in the present article is to bring out these features of the viscoplastic Stokes layer. A main aim is to explore whether the configuration can actually be used as a useful rheometer, much as has been suggested for granular layers [6]. This unconventional forcing in rheometry, which couples oscillating motion and inertia, could serve as a test for rheological models of complex fluids. To this end, we explore the problem both theoretically and experimentally. The theory solves the one-dimensional flow problem, using the Herschel–Bulkley model to represent the viscoplastic rheology (Section 2). The experiment involves driving back and forth a tank filled with an aqueous concentrated suspension of kaolin (Section 3).
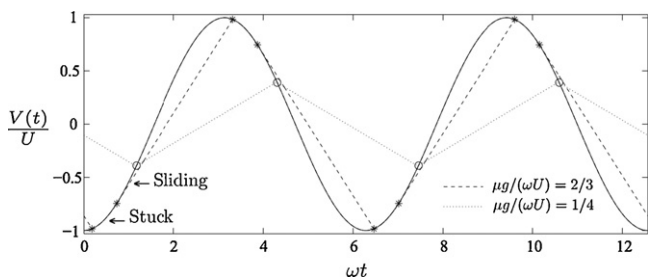

Fig. 2. Periodic solutions to the sliding block model with $\mu g/(\omega U) = 2/3$ (dashed line) or $1/4$ (dotted line). The solid line is the dimensionless plate speed, $-\cos \omega t$. The stars show the moments of the $\mu g/(\omega U) = 2/3$ cycle where the block locks onto or unlocks from the plate. The circles show the instants of acceleration reversal for the $\mu g/(\omega U) = 1/4$ cycle as the relative speed of the plate and block switches sign.

2. Theory

2.1. Governing equations

We solve the unsteady, one-dimensional flow problem sketched in Fig. 1: a plate lying along the x-axis of a two-dimensional coordinate system oscillates sinusoidally with speed, $-U \cos \omega t$, and frequency, ω. For solutions invariant in the x-direction, mass balance requires that the only non-zero velocity component is along x. The flow field induced in the fluid, $u(y,t)$, then satisfies

$$\rho \frac{\partial u}{\partial t} = \frac{\partial \tau}{\partial y}, \tag{4}$$

where ρ is density and τ is the shear stress, which is related to the shear rate u_y by a viscoplastic constitutive law

$$\begin{aligned} u_y &= 0, & |\tau| &< \tau_Y, \\ \tau &= \eta u_y + \tau_Y \ sgn(u_y), & |\tau| &\geq \tau_Y, \end{aligned} \tag{5}$$

with η the viscosity and τ_Y the yield stress. We consider the Herschel–Bulkley model for illustration: $\eta = K|u_y|^{n-1}$, where K and n represent material constants.

The upper surface of the fluid, located at $y = h$, is free, implying that $\tau(h,t) = 0$, and no-slip on the plate demands $u(0,t) = -U \cos \omega t$. The initial condition has the fluid moving rigidly with the plate, $u(y,0) = -U$.

2.2. Dimensional considerations

The preceding formulation contains five dimensional quantities with dimensions involving space and time: U, ω, h, τ_Y/ρ and a characteristic kinematic viscosity, η_*/ρ (where η_* is the usual viscosity for the Bingham model with $n = 1$; when $n \neq 1$, an analogous characteristic viscosity can be built from K and the other constants). At first sight, one might imagine that this would imply that there are three dimensionless groups, plus n, which control the flow dynamics. In particular, since η_*/ρ and ω can be used to construct the Stokes length

$$\ell = \sqrt{\frac{\eta_*}{\rho \omega}} \equiv \left(\frac{K}{\rho \omega}\right)^{2/(n+1)} U^{(n-1)/(n+1)} \tag{6}$$

(with a suitable definition of η_*), there is a length ratio and "Bingham number"

$$H = \frac{h}{l} \quad \text{and} \quad B = \frac{\tau_Y}{\rho \omega \ell U}. \tag{7}$$

The third dimensional grouping can be taken to be the speed ratio, $\omega \ell / U$. However, in the one-dimensional problem under consideration, this last dimensionless number can be dropped using the following dimensionless variables:

$$\hat{t} = \omega t, \qquad \hat{y} = \frac{y}{l}, \qquad H = \frac{h}{l}, \qquad \hat{u} = \frac{u}{U}, \qquad \hat{\tau} = \frac{\tau}{\rho \omega U \ell}, \tag{8}$$

In this choice of dimensionless variables, the velocity scale U is not equal to the time scale $1/\omega$ times the length scale ℓ, which is possible because the horizontal dimension x does not appear in Eq. (4). Consequently, the flow dynamics depends only on H, B and n.

With these choices, using the shear stress as the main dependent variable, and after dropping the hat decoration, we arrive at

$$\frac{\partial}{\partial t} \dot{\gamma}(\tau) = \tau_{yy}, \qquad \tau_y(0, t) = \sin t, \qquad \tau(H, t) = 0, \qquad \tau(y, 0) = 0, \tag{9}$$

where $\dot{\gamma}(\tau)$ is the shear rate written in terms of τ; *i.e.* the inverse of the constitutive law

$$u_y = \dot{\gamma}(\tau) = [\text{Max}(0, |\tau| - B)]^{1/n} \ sgn(\tau). \tag{10}$$

A formulation using τ has the advantage of expressing the shear rate unambiguously in terms of a single-valued function of the shear stress, and comprises a generalized type of Stefan problem [7]. We solve (9) and (10) numerically using the methods outlined in Appendix A.

2.3. The superficial plug and the shear-flow threshold

The stress-free surface boundary condition, $\tau(H,t) = 0$, implies that the stresses within the viscoplastic Stokes layer must always fall below the yield value sufficiently close to the surface. If we denote $y = Y(t)$ as the yield level immediately beneath the surface, then the momentum equation, $u_t = \tau_y$, integrated over the superficial plug implies that

$$(H - Y)\frac{dV}{dt} = [\tau]_{y=Y}^{y=H} \equiv -B \ sgn[\tau(Y, t)], \tag{11}$$

where $u(y,t) \equiv V(t)$ is the surface and plug speed. Eq. (11) also implies the conditions

$$|\tau(Y, t)| = B, \qquad \tau_y(Y, t) = -\frac{B \ sgn[\tau(Y, t)]}{H - Y}; \tag{12}$$

above $z = Y$, the stress solution takes the relatively simple form

$$\tau = B\left(1 - \frac{y}{H}\right) \ sgn[\tau(Y, t)]. \tag{13}$$

Eq. (13) implies that the stress increases linearly with depth until it reaches the yield value at $y = Y$. In fact, the basal shear stress must exceed the yield stress at some moment during the cycle in order that the fluid yield at all. When the whole layer is rigid, the stress distribution is $\tau = (1 - y/H)\sin t$, which is always below the yield stress if $B > H$, *i.e.* $\rho h \omega U < \tau_Y$. In other words, the layer behaves like a rigid block if the inertial force on the entire layer is smaller than the yield stress. Above this threshold, the fluid must yield for
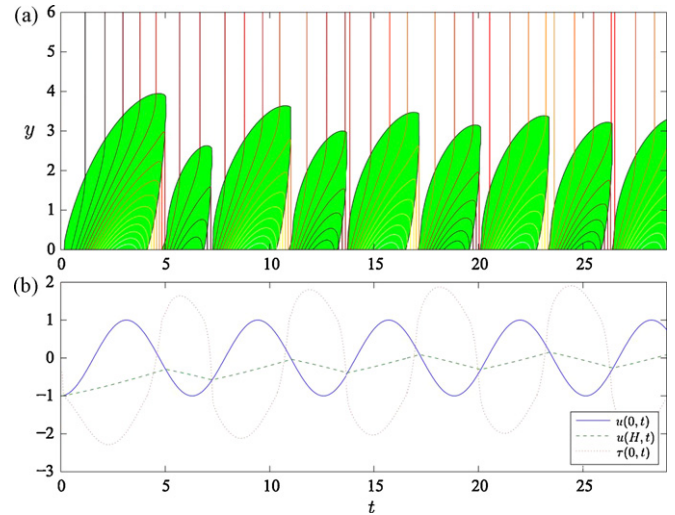
Fig. 3. Initial-value problem beginning with the unstressed state ($\tau(y,0) = 0$ and $u(y,0) = -1$), for $H = 10$, $B = 1$. Panel (a) shows contours of constant $u(y,t)$ (increments of 0.1333 from -1 to 1), with the yielded zones shaded. Panel (b) displays the basal and surface speeds, $u(0,t)$ and $u(H,t)$, as well as the basal shear stress, $\tau(0,t)$.

at least part of the cycle, and over at least part of its depth. However, without solving the equations we cannot gauge the degree of yielding, or its spatial structure as there may be multiple interlaced yielded zones and plugs.

Note that either of the relations in (12) can be used to reduce the size of the computational domain: in principle, the first could be used in conjunction with a front-tracking scheme to avoid computing the overlying plug zone. The second allows one to place an artificial boundary inside the plug at a level which is well below the surface. The first approach must still cope with any other yield surfaces and so we have not proceeded down that pathway; the second scheme proves useful when considering very deep layers.
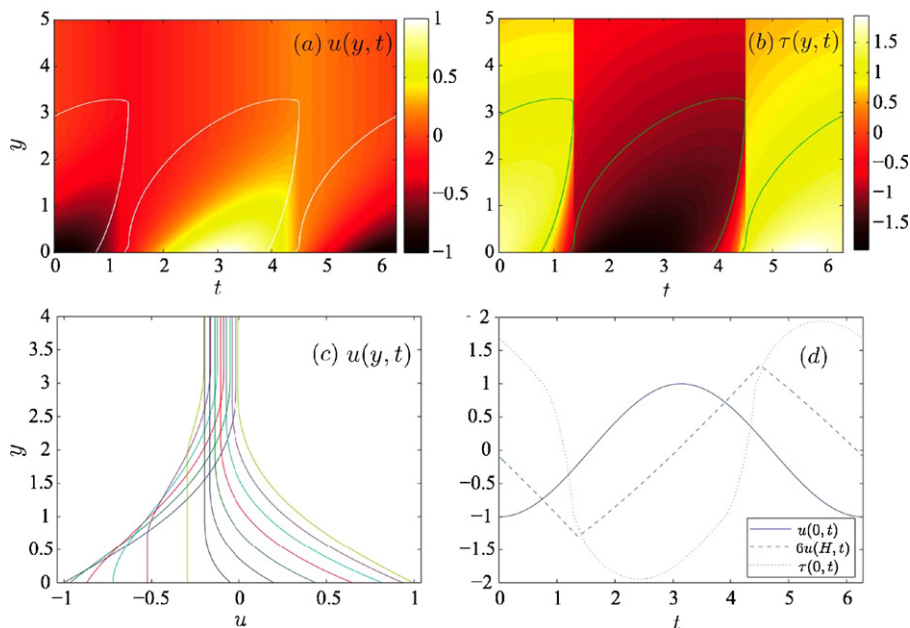
Fig. 4. The final periodic solution for $H = 10$, $B = 1$. Panels (a) and (b) show the speed, u, and shear stress, τ, as densities on the (t,y)-plane (with the yielded zone indicated). Panel (c) shows 13 equally spaced snapshots of $u(y,t)$ through half of its cycle. Panel (d) displays the basal and surface speeds, $u(0,t)$ and $u(H,t)$, as well as the basal shear stress, $\tau(0,t)$.
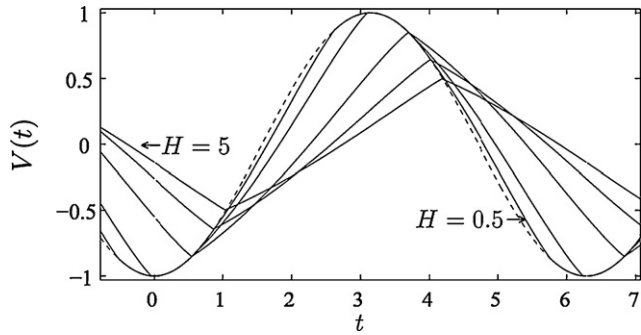
Fig. 5. Surface speed, $V(t)$, against time for $B = 1$ and five values of H (1/2, 2, 3, 4 and 5). The dashed curve shows the sinusoidal oscillation of the base plate.

2.4. Results for the Bingham fluid (n = 1)

A sample solution to the initial-value problem beginning with the unstressed state ($\tau(y,0) = 0$) is shown in Fig. 3. The whole fluid layer initially moves rigidly with the plate, but soon afterwards the bottom regions yield locally as the basal acceleration increases. The yielded zone grows with time until shortly after the plate reverses direction, whereafter it shrinks and eventually disappears near $t = 5$. By that moment, however, a new yielded zone has spawned near the plate which grows to continue the cycle. Eventually the solution converges to a periodic orbit, further details of which are shown in Fig. 4; the yielded zones are localized in both space and time, and two distinct plug regions coexist during part of the cycle. Note the discontinuous change in the shear stress at the moments that a yielded zone collapses (as predicted in a related analysis [8]).

Convenient diagnostics of the dynamics can be extracted from the surface speed, $V(t) = u(H,t)$; see Fig. 5. For the smaller layer depths, the fluid remains rigid throughout its depth for a significant fraction of the cycle, and the surface speed is frozen to the plate forcing. For the larger values of H, the yielded regions expand such that the fluid is yielded somewhere for each instant during the cycle, and $V(t)$ is never locked to the plate. Instead, $V(t)$ begins to resemble a sawtooth profile, despite the sinusoidal forcing, much like the sliding block described in Section 1. This feature can be rationalized from (11) which implies that, if the plug zone is relatively deep, $H \gg Y$ and

$$\frac{dV}{dt} \approx \frac{B}{H} \rightarrow V \approx V_0 \pm \frac{tB}{H}, \qquad (14)$$

for some integration constant, V_0. Moreover, since the cycle period must be 2π, it immediately follows that the peak surface speed is

$$V_{\max} \approx \frac{\pi B}{2H}. \qquad (15)$$

Further details of the surface speed diagnostic for $B = 1$ and varying H are shown in Fig. 6. This picture displays how the maximum values of $|V(t)|$ and $|V(t) + \cos t|$ (the basal-surface velocity difference) vary with H, and also indicates the phase of the cycle at which the maxima occur. For lower H, the speed maximum occurs when the layer is rigid, giving a maximum of unity at zero phase. For larger H, the peak value converges to that expected for the saw-
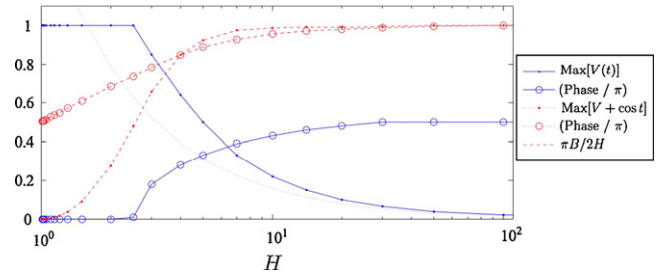

Fig. 6. Plots of the maximum surface speed and the maximum of the departure of that speed from the basal speed, Max($|V + \cos t|$), for $B = 1$. Also indicated is the prediction (15) and the phases of the cycle at which the two maxima occur.

tooth, and the phase approaches $\pi/2$. For the velocity difference, the maximum occurs near $\pi/2$ for small $H - B$, which is the phase of the cycle where the acceleration is largest. As H becomes large, the phase of the maximum velocity difference approaches π, corresponding to the phase of maximum basal speed, which dominates the surface speed in this limit.

3. Experiments

3.1. Set-up and procedure

To compare with the theory, we perform experiments using kaolin slurries (natural clay) as model viscoplastic fluids. This material is well-known to exhibit a yield stress and its rheological properties can be tuned by changing the concentration of kaolin particles in water (e.g. [9]). Another advantage of kaolin slurry in our oscillating configuration is that it is relatively stiff compared with other, softer yield-stress fluids such as Carbopol or Laponite, and so elastic effects are likely minimized. Three different fluid samples were prepared by mixing 48%, 50% and 54% of kaolin (by mass) into distilled water at ambient temperature ($T = 24\,^\circ$C). The rheological behaviour of each solution was measured in a cone-and-plate geometry (Anton-Paar MCR 501) using slightly roughened surfaces and special care was taken in order to prevent evaporation during the tests. Fig. 7 shows that, for each sample, the steady-state flow curve can be approximated by a Herschel–Bulkley fit (see Table 1), suggesting that kaolin slurry is a good choice to compare with the theory. Nevertheless, deviations from the ideal viscoplastic behaviour exist, particularly close to the flow threshold, where creeping, aging and hysteresis are observed. We will return to this point below.

The experimental set-up is sketched in Fig. 8. It consists of a transparent rectangular box made of Plexiglass with a bottom roughened with sandpaper (length 20 cm, width 8 cm, height 4 cm), which is partially filled with a uniform layer of kaolin slurry and enclosed with a transparent film to prevent evaporation. The box is constrained to move horizontally and driven sinusoidally by an electromagnetic shaker with an amplitude, A (0.1 cm < A < 1 cm), and a frequency, ω (1 Hz < $\omega/2\pi$ < 15 Hz). Efforts were made to produce a clean sinusoidal signal, as the dynamics of the mud layer is entirely controlled by the acceleration of the box, which in turn

Table 1
Different experimental conditions used in the experiments

Number of run	% of clay (in mass)	τ_c (Pa)	K (Pa s^n)	n	ρ (g/cm^3)	h (cm)
1	48	16 ± 2	15.5	0.32	1.4 ± 0.1	2.2 ± 0.1
2	48	16 ± 2	15.5	0.32	1.4 ± 0.1	1.1 ± 0.1
3	50	20 ± 3	17	0.3	1.4 ± 0.1	1.45 ± 0.1
4	54	40 ± 5	36.4	0.35	1.6 ± 0.1	1 ± 0.1

τ_c, K and n are the parameters of the Herschel–Bulkley fit.
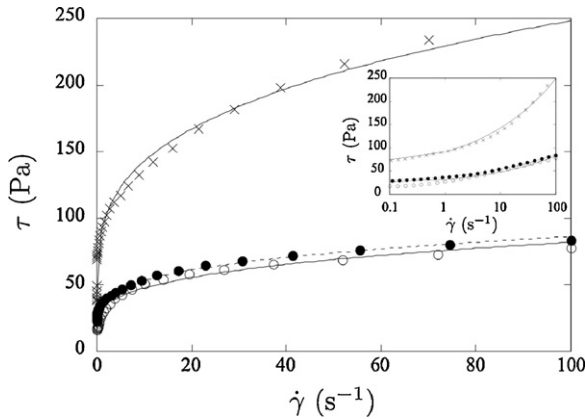
Fig. 7. Flow curves for the kaolin slurries ((◯) 48%, (●) 50%, (×) 54% of kaolin particles in mass) obtained by decreasing the shear rate after an initial preshear (log-ramp in the range of 100–10^{-2} s^{-1}, for waiting time in the range of 1–100 s). The lines correspond to the Herschel–Bulkley fit.

Fig. 9. Amplitude of the surface displacement in the moving frame, $\Delta X = \langle [X(t) - X_b(t) - \langle X(t) - X_b(t) \rangle]^2 \rangle^{1/2}$, over the Stokes length l, as a function of H/B. Data obtained for run 1 by increasing A at different frequencies. *Inset*: phase difference between the free surface displacement $X(t)$ and the base displacement $X_b(t)$, computed using the Fourier transform of both signals.

is sensitive to small imperfections in displacement. The motion of the fluid surface, $X(t)$, is measured by tracking with a high-speed camera (1000 fps) the position of a 5 mm diameter tracer. The motion of the box, $X_b(t)$, is recorded simultaneously using a reference marker rigidly fixed to the box (Fig. 8). The positions of both tracers are obtained to within a precision of 50 μm. We checked that the motion of the free-surface is not affected by the side-walls, except close to the edges where a thin boundary layer of order h existed. All measurements are made at the centre of the box.

3.2. Results

We first studied the onset of motion of the mud layer. In the theory, the threshold is controlled by a single dimensionless number, $H/B = \rho \omega h U / \tau_c = 1$. As a first test, we consider a given slurry with one depth (run 1 in Table 1), and vary the amplitude of the box motion, $A = U/\omega$, for different frequencies. Fig. 9 shows how the amplitude of the relative surface displacement vary with H/B. The inset also shows the phase lag that appears between the surface displacement and the base displacement. At low forcing amplitudes (or H/B), the fluid layer oscillates in solid motion with the box, and both displacements are equal and occur at the same phase. At higher amplitudes, the free-surface displacement no longer follows the base and a phase lag arises, indicating that the fluid is now sheared. Although the critical driving amplitude for the flow threshold depends upon frequency, each threshold corresponds to $H/B = 1$, as shown by Fig. 9. The same result is obtained when both the layer depth and the yield-stress are varied, as shown in Fig. 10. In all cases, the mud layer is rigid below $H/B = 1$ and starts to flow for $H/B > 1$.

Typical time series of the free-surface speed are displayed in Fig. 11 for different values of H/B. Close to the flow onset (Fig. 11a), the fluid motion is characterized by a sticking phase where the fluid
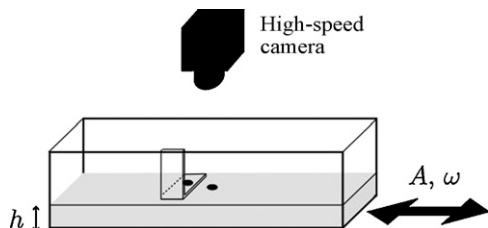
moves rigidly with the plate followed by a slip motion. This stick-and-slip behaviour can be highlighted on plotting the relative speed between the mud surface and the base (Fig. 12). As we move further from the threshold, the sticking phase disappears and a phase lag arises between the two signals (Fig. 11b and c). Note that during the cycle, the mud surface reaches speeds that are higher than the base speeds. This effect occurs close to the flow threshold, but disappears at larger driving amplitudes (Fig. 11d and e). The overshoot is systematically observed for all the flow conditions we have tested, as shown by Fig. 13 where the ratio of the maximum surface speed and U is plotted versus H/B.

3.3. Comparison

The experimental observations are in partial agreement with the visco-plastic theory developed in Section 2. First, the flow threshold is well reproduced by the criterion, $H/B = 1$, and the slurry behaves like a rigid block below this threshold. Second, just above the flow threshold, a stick-slip regime is observed in both experiment and theory. Third, the observed surface speed decreases at large driving, as predicted by the theory. Despite this, the theory fails to qualitatively capture the detailed dynamics observed experimentally, even though the flow curves measured in the rheometer are well described by the Herschel–Bulkley fit. In particular, the time series of the observed surface speeds shown in Fig. 11 are qualitatively different in shape from their theoretical counterparts (included in the same figure); at larger driving, theory predicts a sawtooth-like
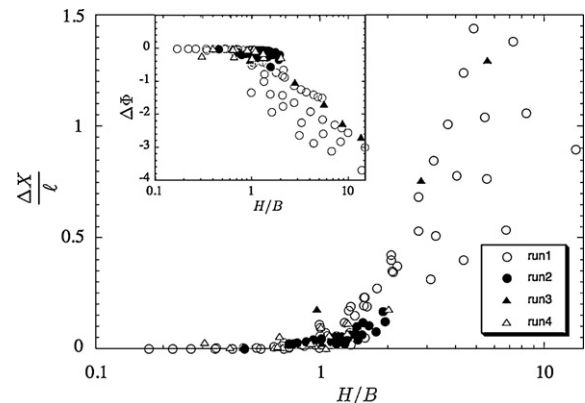

Fig. 8. Sketch of the experimental set-up.

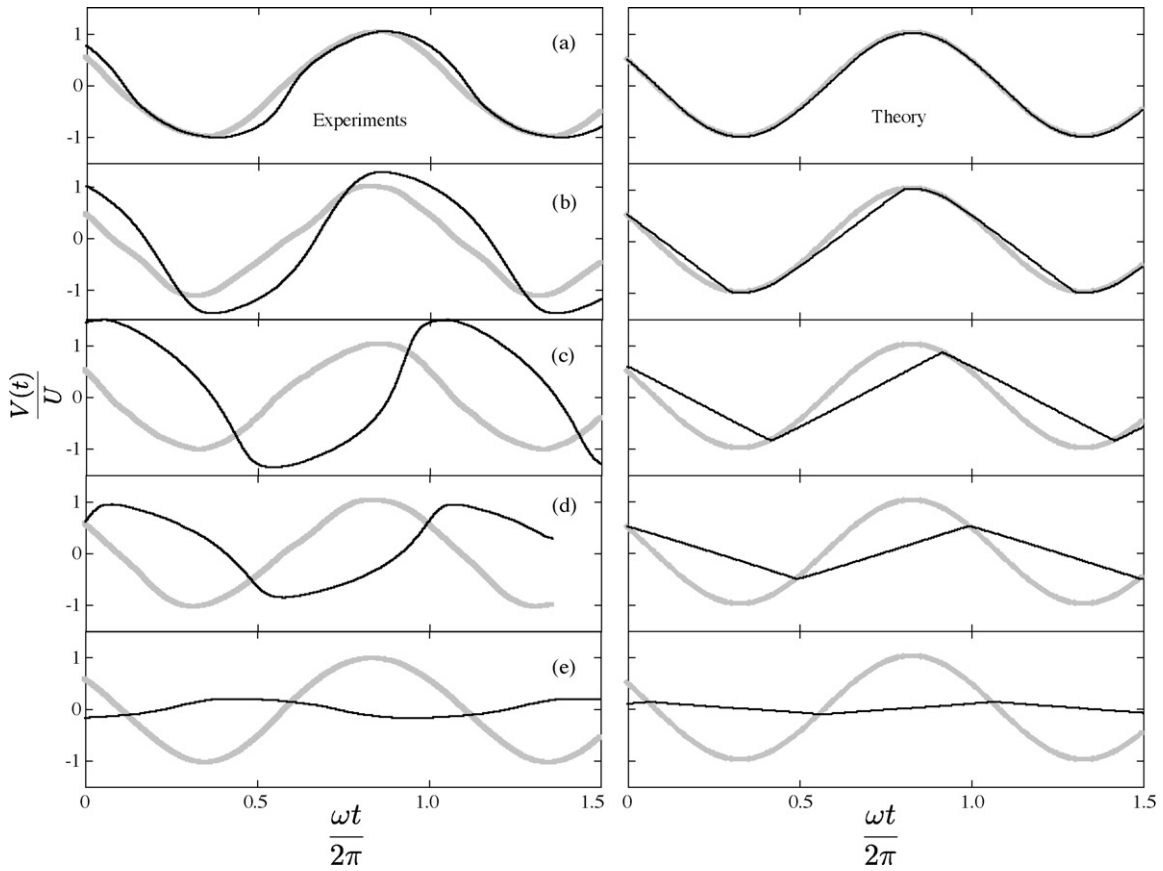**Fig. 10.** A picture similar to Fig. 9, but including all the experimental runs of Table 1.

Fig. 11. Examples of experimental (left) and theoretical (right) time evolution of the free surface speed (the reference base velocity is plotted in grey); (a) $H = 2.49$, $B = 1.9$, $H/B = 1.32$; (b) $H = 9.3$, $B = 6.5$, $H/B = 1.43$; (c) $H = 13.3$, $B = 6.3$, $H/B = 2$; (d) $H = 10.7$, $B = 2.6$, $H/B = 4.1$; (e) $H = 18.1$, $B = .86$, $H/B = 21$. For the theory, $n = 1/3$.
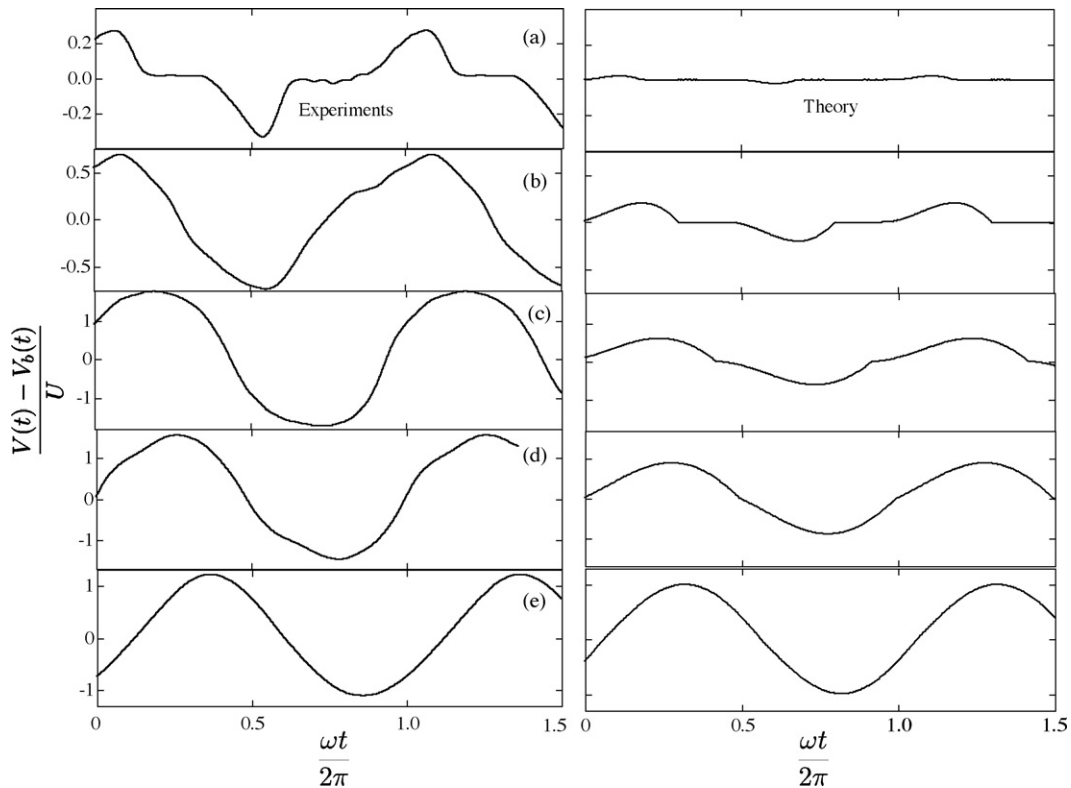

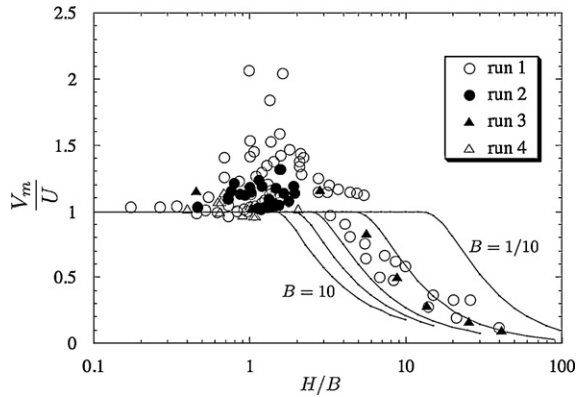**Fig. 12.** Same as Fig. 11 for the relative velocity.

Fig. 13. Maximum free surface speed, $V_m = \mathrm{Max}(V)$, normalized by U, as a function of H/B. *Symbols*: experiments, the different flow conditions are given in Table 1. *Solid lines*: theory for five values of B (1/10, 1/3, 1, 2 and 10), and $n = 1/3$.

variation whereas the observations display more structure. More strikingly, the theory always predicts that $U > |V(t)|$, whereas close to the threshold, the mud surface speed is observed to be systematically larger than U (Fig. 13).

The fact that the surface speed overshoots the forcing close to the flow threshold could suggest that some sort of resonance is taking place. Two possibilities present themselves: resonance with an elastic standing wave or a gravity wave. An elastic origin, however, does not seem plausible in view of the fact that below the threshold, no relative motion between the free surface and the base is detectable, indicating that elastic deformations are insignificant. Moreover, one can estimate a characteristic resonance frequency based on the time taken for an elastic wave to traverse a layer of depth h: $t_{el} = h/\sqrt{E/\rho}$, where E is Young's modulus. With measurements of $E = 10^4$ Pa, based on oscillatory tests in a rheometer, we estimate $t_{el} = 4$ ms, which is much smaller than any of the experimental oscillation periods. Likewise, we can also dismiss resonance with a surface gravity wave since the dynamics is unaltered when we used different depths, lengths and widths (which should change the mode frequency).

We conclude that the origin of the discrepancy lies in the unsteady rheological properties of the kaolin slurry. Thixotropy, which is known to occur in natural clays, could be the explanation [10]. It is well known that dense colloidal suspensions exhibits aging. The material does not becomes instantaneously rigid when stress becomes less than the threshold but takes a finite time to recover its rigidity. In our configuration, the stress periodically crosses the threshold value. The recovery time could then play an important role. However, the forcing periods in the experiment are relatively rapid in comparison to the relaxation times normally considered to characterize thixotropy in slurries. A second source of thixotropic effect could arise from a flow-induced orientation of the microstructure [11]. In our experiment the stress not only periodically crosses the threshold, but changes sign. The reorientation of the microstructure when shear changes sign could transiently soften the material, which could explain the amplitude overshoot observed experimentally. Further investigation is necessary to discriminate between these different hypothesis.

4. Conclusions

We have presented a theoretical and experimental exploration into the effect of viscoplasticity on the dynamics of the Stokes layer. Theoretically, we find that the yield stress introduces a complicated spatio-temporal pattern of yielded zones and plugs within the fluid layer. However, overall, and as anticipated, the dynamics interpo-

lates between the viscous Stokes layer and a sliding rigid block as the effect of the yield stress is increased.

Rather surprisingly, although in the experiment we use a fluid that is seemingly well described by the Herschel–Bulkley flow rule, we discover qualitative disagreement between theory and experiment. More specifically, we have found that shaking a kaolin slurry leads to an excitation of fluid activity that is both more pronounced and richer than expected. We suspect that this reflects some significant relaxational dynamics in the fluid which is not captured by the steady flow rule. Our flow is highly unsteady with a shear rate that changes sign periodically; therefore its dynamics could be highly coupled to internal relaxation modes, such as thixotropic and microstructure orientation effects [11].

We set out in this study with the hope that the viscoplastic Stokes layer might prove to be a valuable rheological device. Although we leave the reader with an unsatisfying disagreement between theory and experiment, this hope seems to have been borne out: unexpected dynamical features have been revealed by the viscoplastic Stokes layer, that could serve as a test to probe more elaborated rheological models [12,13].

Appendix A. Solution method

We solve (9) and (10) numerically using a standard implicit or a simpler semi-implicit scheme in time. Spatial derivatives are dealt with *via* either second-order-accurate finite differences on either a fixed or moving grid (the latter adapted from [14]). The implicit time integrators are based around the differential-algebraic solver DASSL [15]. In principle, a fully implicit scheme can deal with a yield surface moving across the grid. However, most state-of-the-art implicit solvers also require iteration to the solution, which is problematic in the current problem at the instants when spatially localized yielded regions or plugs collapse (yield surfaces collide; see Section 2). At that instant, the stress solution is formally discontinuous, which can make an iterative scheme fail to converge. On the other hand, a scheme that suspends the iteration or proceeds explicitly will jump across the moment of discontinuity and thereby incur error. We avoid the problem in the iterative schemes by "regularizing" the problem and smoothing out the function, $\dot{\gamma}(\tau)$, using the convenient (but rather arbitrary) construction:

$$\frac{\partial}{\partial t}\dot{\gamma}(\tau) = \dot{\gamma}'(\tau)\tau_t \equiv \tau_t \left[1 + \frac{\tau^2 - B^2}{\sqrt{\varepsilon^2 + (\tau^2 - B^2)^2}} \right], \qquad (A.1)$$

with ε chosen to be as small as possible (typically less than 10^{-6}, and no greater than 10^{-4} in the worst cases).

The simpler finite-difference, non-iterative, semi-implicit scheme is formulated as follows (Pailha and Pouliquen, in preparation)

$$\dot{\gamma}_t \approx \frac{\dot{\gamma}_j^{n+1} - \dot{\gamma}_j^n}{dt} \approx \frac{\tau_{j+1}^n + \tau_{j-1}^n - 2\tau_j^{n+1}}{dx^2} \qquad (A.2)$$

where j refers to the jth grid point and n to the nth time step, and dt and dx are the time step and grid spacing (with appropriate modifications to incorporate the end points). In other words, the second

derivative is dealt with semi-implicity in such a way that we may write an equation for the evolved shear stress:

$$\tau_j^{n+1} + \frac{2\mathrm{d}x^2}{\mathrm{d}t}\dot{\gamma}_j^{n+1} = \frac{1}{2}(\tau_{j+1}^n + \tau_{j-1}^n) + \frac{2\mathrm{d}x^2}{\mathrm{d}t}\dot{\gamma}_j^n \equiv J_j^n. \qquad (A.3)$$

If $|J_j^n| < B$ or $\mu_1(1 - y/H)$, the jth grid point is unyielded and we set $\tau_j^{n+1} = J_j^n$; otherwise we include $\dot{\gamma}_j^{n+1}$ and solve algebraically for τ_j^{n+1}. This solver needs no regularization. However, the semi-implicit fashion in which the second derivative is dealt with has the disadvantage of additional smoothing, which acts much the same as the regularization of the implicit schemes.

We verified that the various schemes gave identical results for the computations reported in the main text. However, a better procedure would be to integrate forwards upto and not beyond the moment that the yielded zone disappears. The integration could then be restarted with the jump in τ taken into account [8]. One of the referees (Professor J. Billingham) also kindly confirmed the results with a specially designed implicit algorithm incorporating no regularization.

References

[1] G.K. Batchelor, Fluid Dynamics, Cambridge University Press, 1967.
[2] S.H. Davis, The stability of time-periodic flows, Ann. Rev. Fluid Mech. 8 (1976) 57–74.
[3] V. Yakhot, C. Colosqui, Stokes' second flow problem in a high-frequency limit: application to nanomechanical resonators, J. Fluid Mech. 586 (2007) 249–258.
[4] K.R. Rajagopal, A note on unsteady unidirectional flows of a non-Newtonian fluid, Int. J. Nonlinear Mech. 17 (1982) 369–373.
[5] T. Hayat, S. Asghar, A.M. Siddiqui, Stoke's second problem for a Johnson–Segalman fluid, Appl. Math. Comput. 148 (2004) 697–706.
[6] S. Aumaitre, C. Puls, J.N. MacElwaine, J.P. Gollub, Comparing flow thresholds and dynamics for oscillating and inclined granular layers, Phys. Rev. E 75 (2007) 061307.
[7] E. Comparini, A one-dimensional Bingham flow, J. Math. Anal. Appl. 167 (1992) 129–139.
[8] E. Comparini, E. De Angelis, Flow of a Bingham fluid in a concentric cylinder viscometer, Adv. Math. Sci. Appl. 6 (1996) 97–116.
[9] P. Coussot, Mudflow rheology and dynamics, IAHR Monograph Series, Balkema, 1997.
[10] H.A. Barnes, Thixotropy-a review, J. Non-Newtonian Fluid Mech. 70 (1997) 1–33.
[11] F. Pignon, A. Magnin, J.-M. Piau, Butterfly light scattering pattern and rheology of a sheared thixotropic clay gel, Phys. Rev. Lett. 79 (1997) 4689–4692.
[12] N. Roussel, R. Le Roy, P. Coussot, Thixotropy modelling at local and macroscopic scales, J. Non-Newtonian Fluid Mech. 117 (2004) 85–95.
[13] J. Billigham, J.W.J. Feguson, Laminar, unidirectional flow of a thixotropic fluid in a circular pipe, J. Non-Newtonian Fluid Mech. 47 (1993) 21–55.
[14] J.G. Blom, P.A. Zegeling, Algorithm 731: a moving-grid interface for systems of one-dimensional time-dependent partial differential equations, ACM Trans. Math. Softw. 20 (1994) 194–214.
[15] L. Petzold, A description of DASSL: a differential/algebraic systems solver, in IMACS Trans. Sci. Comp., vol. 1, R.S. Steplman (Ed.), North-Holland, Amsterdam, 1983.